JGR Planets

RESEARCH ARTICLE
10.1029/2022JE007264

Melt Production and Ejection From Lunar Intermediate-Sized Impact Craters: Where Is the Molten Material Deposited?

T. Liu[1], R. Luther[1], L. Manske[1,2], and K. Wünnemann[1,2]

[1]Museum für Naturkunde Berlin, Leibniz Institute for Evolution and Biodiversity Science, Berlin, Germany, [2]Freie Universität Berlin, Berlin, Germany

Key Points:

- The melt concentration in the ejecta blanket increases almost linearly with distance from the crater center
- Near-surface porosity causes an increase in melt production. Due to decreasing porosity with depth, it is more prominent at small craters
- The melt concentration in distal ejecta of crater of 10's km is rather high (>30%)

Supporting Information:

Supporting Information may be found in the online version of this article.

Correspondence to:

T. Liu,
Tiantian.Liu@mfn.berlin

Citation:

Liu, T., Luther, R., Manske, L., & Wünnemann, K. (2022). Melt production and ejection from lunar intermediate-sized impact craters: Where is the molten material deposited? *Journal of Geophysical Research: Planets*, *127*, e2022JE007264. https://doi.org/10.1029/2022JE007264

Received 24 FEB 2022
Accepted 9 JUL 2022

Author Contributions:

Conceptualization: T. Liu, R. Luther, K. Wünnemann
Funding acquisition: K. Wünnemann
Methodology: T. Liu, R. Luther, L. Manske
Supervision: R. Luther, K. Wünnemann
Validation: T. Liu
Writing – original draft: T. Liu
Writing – review & editing: T. Liu, R. Luther, L. Manske, K. Wünnemann

Abstract Differently aged impact melt in lunar samples is key to unveiling the early bombardment history of the Moon. Due to the mixing of melt products ejected from distant craters, the interpretations of the origin of lunar samples are difficult. We use numerical modeling for a better quantitative understanding of the production of impact-induced melt and in particular its distribution in ejecta blankets for lunar craters with sizes ranging from 1.5 to 50 km. We approximate the lunar stratigraphy with a porosity gradient, which represents the gradual transition from upper regolith via megaregolith to the solid crustal material. For this lunar setting, we quantify the melt production relative to crater volume and derive parameters describing its increasing trend with increasing transient crater size. We found that about 30%–40% of the produced melt is ejected from the crater. The melt concentration in the ejecta blanket increases almost linearly with distance from the crater center, while the thickness of the ejecta blanket decreases following a power law. Our study demonstrates that if in lunar samples the concentration of a melt with a certain age is interpreted to be of a nonlocal origin, these melts could be the impact products of a large crater (>10 km) located hundreds of kilometers away.

Plain Language Summary Lunar samples contain abundant impact-induced melt that crystallized at different ages. The melt ages record the formation time of its source craters and are key for a better understanding of the lunar bombardment history. In samples, there is not only the melt derived from the sampling region but also some that originate far away by being entrained in the ejecta of distant craters. Recognizing the distant-derived melt is essential for the more credible sample interpretation, which requires knowledge of the melt distribution in the ejecta. We use numerical modeling to quantify the production of impact-induced melt and in particular its distribution in ejecta blankets for lunar craters. We found that the melt concentration in the ejecta blanket increases with distance from the crater center. If the concentration of distant-derived melt of a certain age in lunar samples is rather high (>30%), it could originate from large craters (>10 km) located hundreds of kilometers away.

1. Introduction

Impact-induced melting has been a fundamental process throughout the lunar history. Due to high temperatures as a consequence of shock heating in hypervelocity impact events (commonly 18 km/s on the Moon; Ivanov, 2001; Marchi et al., 2009), the radioisotopic clock of lunar impact melt rocks is reset recording the formation time of impact events. Melt-bearing impactites are common in the lunar sample collection and some lunar meteorites. Up to 50% of soils and highland hand specimens are impact melt glasses and rocks (Vaniman et al., 1991). Some melts are thought to be the products of a few large impact basins (Stöffler, 2006). By relating impact melt to specific basin-forming events, the age of impact melt defines the formation time of the related basins, which is key to constraint on the lunar chronology system (Stöffler, 2006) and the reconstruction of the lunar bombardment history (Kring & Cohen, 2002). Both, however, are still under debate mainly due to the difficulty to interpret the origin of the collected impact melt. Being entrained in the ejecta, some melt products could be derived from locations that are rather distant from the sampling sites. Understanding how impact melt is distributed in ejecta is, therefore, important for interpretations of the geological context regarding the bombardment history of lunar samples.

The production of impact-induced melt has been extensively studied using theoretical scaling laws, numerical modeling, and field observations (of terrestrial craters) (Bjorkman & Holsapple, 1987; Cintala & Grieve, 1998; Grieve & Cintala, 1992; Pierazzo & Melosh, 2000; Pierazzo et al., 1997). However, the estimates presented in these studies show distinct differences. Impact melt volumes measured in terrestrial impact structures differ by

up to 2–7 times the values predicted by scaling laws. Previous studies (Cintala & Grieve, 1998; Dence, 1971) suggest that a generally small proportion of impact melt is excavated from the crater; however, the quantitative distribution of impact melt in ejecta has not been systematically investigated. This is because of the relatively poor preservation of ejecta deposits caused by the modification of subsequent volcanic flows, impact gardening, and for terrestrial structures, also by erosion. Besides the distribution of impact melt, it is also important to account for the presence of target porosity affecting both the ejection and the production of impact-induced melt. By using numerical modeling, Wünnemann et al. (2008) quantified the effect of porosity in terrestrial rocks on the melt production assuming homogeneously porous targets. Recent studies revealed that the lunar crust is heavily fractured down to a depth of ∼30 km showing a distinct porosity gradient with depth (Besserer et al., 2014). In this layer, porosity varies from ∼25% in the near-surface regolith and megaregolith to ∼10% in the middle and lower crust. Therefore, it is likely that the formation of intermediate-sized craters (several km to 10's km in diameter) and related melt production and ejection are affected by porosity. Except for the basin-forming events, these craters are the main source of impact melt on the Moon (Liu et al., 2020, 2021). For a better interpretation of lunar samples, quantifying the production of impact melt in targets with a porosity gradient is hence imperative.

In this study, we use the iSALE shock physics code to investigate the melt production and distribution in intermediate-sized impact cratering events (1.5–50 km in diameter) on the Moon. In Section 2, we describe the method and present the considered porosity profile derived from the lunar gravity observations. Then, we show the derived production of impact-induced melt focusing on the total melt abundance, its dispersion inside and outside the crater, and particularly its concentration in ejecta.

2. Methods

We used the iSALE (2D, Version Dellen) shock physics code (Collins et al., 2004; Wünnemann et al., 2006) to simulate impact processes. The code is based on the SALE hydrocode solution algorithm (Amsden et al., 1980). To simulate hypervelocity impact processes in solid materials, SALE was modified to include an elastoplastic constitutive model, fragmentation models, and various equations of state (EoS). It was later improved by the ε–α porosity compaction model (Collins et al., 2011; Wünnemann et al., 2006). The porosity compaction model has been tested against and compared to mesoscale numerical models that explicitly resolved pore space with a high resolution and experimental data (Collins et al., 2011; Güldemeister et al., 2015; Kowitz et al., 2013; Wünnemann et al., 2016).

The material parameters used for modeling in this study are listed in Table S1 in Supporting Information S1, which closely follow previous studies (Collins et al., 2004; Lompa et al., 2021; Potter et al., 2013). To investigate the melt distribution of intermediate-sized impact events, the diameter of projectiles L ranges from 100 m to 3 km. The impact velocity in our models is 18 km/s according to the average impact velocity on the Moon (Ivanov, 2001). Due to the 2D cylindrically symmetric nature of our model, we consider vertical impact only. We discuss the effect of velocity and impact angle in a separate section further down. We assume a half-space to represent the lunar crust. An analytic equation of state (ANEOS) for basalt is used to describe the thermodynamical behavior of the lunar crust (cf. Pierazzo et al., 2005). Material strength, damage, and porosity were accounted for using the models of Collins et al. (2004), Ivanov et al. (1997), Wünnemann et al. (2006), and Collins et al. (2011), respectively.

2.1. Target Setup

Due to long-term impact-induced fragmentation, the lunar crust is extensively fractured, and porous, where the shallower layers generally possess higher porosities. Besserer et al. (2014) used an exponential function to fit the decrease in porosity with depth that best matches gravity data obtained by the Gravity Recovery and Interior Laboratory (GRAIL) mission. The presence of porosity enhances melt production (Güldemeister et al., 2013; Kowitz et al., 2013; Wünnemann et al., 2008), which may explain the observation that samples of soft lunar regolith are heavily charged with impact melt in contrast to associated solid lunar rocks (Vaniman et al., 1991).

Since intermediate-sized craters mainly form in the near-surface regolith and megaregolith layers of the upper crust, the porosity of the impact target is non-negligible. The porosity profile in our models follows the exponential function suggested by Besserer et al. (2014) with a porosity of ∼25% at the surface (highly porous regolith), a decay to half of the top layer porosity in a depth of 5 km (megaregolith), and full compaction of crustal bedrock in

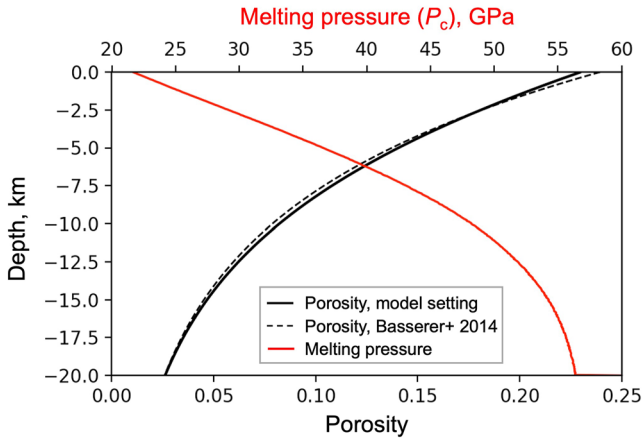

Figure 1. Porosity profile (black) and corresponding critical shock pressure for melting (P_c, red) of basalt with an initial temperature of 250 K and a lithostatic pressure below 0.1 GPa. Impact-induced melts are generated if the target material experiences peak shock pressures (P_{peak}) greater than P_c.

a depth greater than 20 km (Figure 1). Another consequence of the long-term impact fragmentation is the damage of crustal rocks reducing the material strength, that is, the coefficient of friction and cohesion of target rocks. Both have been found to have strong effects on the distribution of ejecta (Luther et al., 2018). To account for the variation of material strength in the different stratigraphic units, we assume the same gradient for the material damage, where the damage equals one at the surface and exponentially decreases with depth.

The volume of the zone where the material experiences sufficiently high shock pressures to cause melting is small relative to the volume of the transient crater and the volume of the excavation zone from where the material is ejected upon the formation of the crater. It is known that this ratio decreases with a decreasing crater size. In other words, the smaller the crater, the smaller the volume of material that experiences melting. The zone of the ejected material that is shock-molten is given by the intersection of the melting zone with the excavation zone, which is even smaller than the entire melting zone. As an example, Figure 2 presents the zones of melting and excavation for an impact of a diameter $L = 1$ km. The strong difference in volume among the melt zone, the excavation zone, and the transient crater cause problems regarding the spatiotemporal resolution. The resolution of iSALE models is commonly related to the size of the projectile and defined by the number of computational cells per projectile radius (CPPR). Due to the small scale of projectiles, the high resolution leads to a large grid of cells, which implies very long computation times.

Most previous studies on impact melt production (Barr & Citron, 2011; Pierazzo et al., 1997; Quintana et al., 2015; Wünnemann et al., 2008) only determined the total volume of shocked melt, which merely requires one to compute the process until the shock wave has attenuated below the critical shock pressure for melting. To investigate the melt production while tracing its distribution in ejecta, both the high resolution and the long run time are required. Keeping the resolution of simulations for the ejection process, the same as for the shock melt determination is computationally expensive, while it does not significantly increase the accuracy of the ejection analysis (Luther et al., 2018). In order to determine the distribution of melt products, the following three processes need to be considered: (a) the zone of shock molten material needs to be determined from the model with a high resolution, (b) the zone of excavation needs to be determined from simulations of the entire ejection process requiring sufficient long run times, and (c) the initial trajectory of ejected material has to be recorded in order to reconstruct the ejecta blanket while tracing the shocked melt.

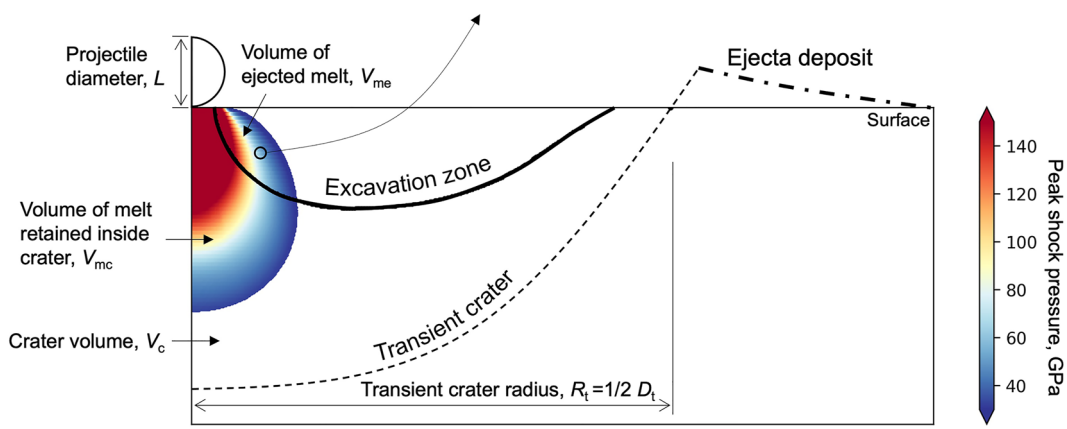

Figure 2. Determination of the shocked melt and definition of variables, where the colored melting zone displays peak shock pressures of impact-induced melt for impact of a diameter $L = 1$ km. The amount of molten material that is ejected outside the crater is given by the intersection of the melting zone with the excavation zone. The residual molten material would remain inside the crater cavity.

To reach a good compromise between computational costs (computation time and memory) and accuracy of the simulations, we employ a 3-step approach for our systematic study: For each projectile size L, both high-resolution models aiming to determine the shock pressure history and low-resolution models aiming to calculate the formation of craters and ejecta are performed: First, we generate separate models for the melt and the ejecta analysis for the same L, for which we apply different model resolutions to match each analysis goal. Then, we combine the results from both models to determine the amount of melt in the ejected material. In the following, we describe each step in more detail (a schematic of 3-step approach is displayed in Figure S1 in Supporting Information S1).

To track the ejected material and its shock history, we use Lagrangian tracers. These tracers are placed in each computational cell initially and represent the matter originally located in that cell throughout the simulation. They are moved with the velocity field of the material flow and record the maximum shock pressure they experience upon shock compression (see Section 2.2.1) and if applicable, ejection velocity and angle during crater formation (see Section 2.2.2).

2.2. 3-Step Approach

2.2.1. Models to Determine Impact-Induced Melting ("Melt Model")

Impact-induced melting in high-velocity impact events is governed by the thermodynamics of shock compression and release. This is a thermodynamically irreversible process in which the release from the maximum shock state behaves isentropically. Depending on the peak shock pressure that the material experiences, its temperature is raised and potentially succeeds the melt temperature (e.g., Figure S2 in Supporting Information S1). To quantify melt production, we follow the commonly used approach and determine the critical shock pressure P_c, where the post-shock final temperature is in excess of the melt temperature (Artemieva & Lunine, 2005; Barr & Citron, 2011; Manske et al., 2021; Pierazzo & Melosh, 2000; Pierazzo et al., 1997; Wünnemann et al., 2008). Impact-induced melts are generated if the material experiences peak shock pressures (P_{peak}) are in excess of P_c. Frictional heating also adds to the total temperature raise during shock compression and release and subsequent deformation. We neglect its contribution in this study since the influence is estimated to be rather small for high-impact velocities (Kurosawa & Genda, 2018; Quintana et al., 2015).

To calculate the thermodynamic state, we follow the assumption that the crushing of pores can be separated from the compression of the solid component (Carroll & Holt, 1972). Güldemeister et al. (2013) and Kowitz et al. (2013) have shown that the crushing of pore space significantly increases local temperatures by the addition from plastic work. As a consequence, smaller critical shock pressures P_c are required to cause melting in porous materials; hence, with increasing porosity P_c decreases. In other words, the more porous the impacted rock, the less shock pressure is required to induce melting. We calculate the minimum shock pressure P_c for which the temperature after isentropic release matches or exceeds the melt temperature following Wünnemann et al. (2008) and Manske et al. (2021). Given the varying porosity with depth, we numerically calculate P_c for materials at certain depths using ANEOS and the ε–α–compaction model (Wünnemann et al., 2006). First, for a given initial porosity, we derive the shock states (temperature and entropy) as a function of the peak shock pressure P_{peak} by calculating the Hugoniot curve. Then, we compute the resulting post-release temperature via the isentropic release curves from these shock states (P_{peak}) back to normal pressure to find the matching peak shock pressures P_c. In this study, we use the solidus function after Katz et al. (2003).

We use tracers to record the P_{peak} the material experiences during the passage of the shock wave. The total melt production is the sum of all tracer masses with $P_{peak} > P_c$. The melt volume is then given by dividing the melt mass by the initial density of the material (basalt, 2,860 kg/m^3, Melosh, 1989) represented by the tracer. Given the presence of porosity, the total volume associated with each tracer corresponds to the bulk volume of the solid component in the uncompacted material. We do not distinguish between melting and vaporization and denote both with "impact-induced melt." However, even though the volume of produced vapors can be large, due to the required high shock pressure for vaporization, its mass is small compared to the mass of the molten material for the average impact velocities on the Moon.

Impact events commonly strike lunar surfaces obliquely. However, the magnitude of impact velocity, rather than the impact angle, is the principal factor governing the production of impact melt (Pierazzo & Melosh, 2000). In our melt models that are designed to record the shock history of impact target, the common impact velocity of 18 km/s is considered. We discuss further down to what extent our results are applicable for varying impact

velocities and impact angle. In addition, it was found that 40 CPPR in iSALE keeps the numerical error on the melt volume <10% (Wünnemann et al., 2008). So, we choose a resolution of 40 CPPR for melt models and simulate only the early stage of the impact process until the shock wave has sufficiently attenuated below P_{peak}. The area where P_{peak} of materials exceeds P_c is used to quantify the abundance of melt (e.g., the colored melting zone for impact of $L = 1$ km in Figure 2).

2.2.2. Models to Analyze Ejecta Deposit ("Ejecta Model")

Lagrangian tracers that follow the excavation flow upon the crater formation are also used to track ejected materials. Tracers are considered to be ejected when they reach the altitude of one projectile radius above the surface (Luther et al., 2018). For each tracer that satisfies this criterion, we record the ejection speed, angle, time, launch position, and mass. Assuming that at this altitude the material is moving ballistically, we extrapolate the trajectory back to the surface. Using these parameters, the parabolic trajectory and the landing distance of each tracer are calculated. This approach has been successfully used for model validation against laboratory experiments (Luther et al., 2018; Raducan et al., 2019; Wünnemann et al., 2016) as well as for the analysis of the formation of lunar basins (Zhu et al., 2017). Luther et al. (2018) applied this approach to conduct a systematic numerical parameter study for a range of target materials with different strength and porosity and determined launch characteristics as well as the deposition of ejected materials.

The cumulative number of tracers deposited at a given distance allows for determining the thickness of the ejecta blanket, assuming a reference density of the ejected material and impact-induced melt equal to the initial density of the material prior to ejection. By radially binning the location of ejecta, we can calculate the surface area of each bin and thus derive the thickness of ejecta deposits in each bin. The density of the deposited material is somewhat smaller than the initial density due to the increase of the porosity and heating (Zhu et al., 2017), but we consider the difference in density to be small and neglect its contribution to the ejecta thickness distribution (e.g., Luther et al., 2018).

The impact angle can have an important effect on the cratering and the ejection process. Housen and Holsapple (2011) summarized and examined laboratory measurements of impact crater ejecta from 18 studies to assess how the ejecta distributions depend on the conditions of an impact event. They conclude that while distal ejecta have a definite dependence on the impact angle, the ejecta deposited within several crater radii may scale as a vertical impact using the normal component of the impact velocity. Consequently, in our iSALE-2D models that are designed to analyze the ejection behavior, we use an impact velocity of 13 km/s, which is the normal component of impact speed for the most likely impact angle on the Moon of 45° (Elbeshausen et al., 2009; Ivanov, 2001). We use a resolution of 10 CPPR, which is sufficient to simulate crater growth (Wünnemann et al., 2008) and the general ejection behavior (Luther et al., 2018). The ejecta models are run until the crater reaches the maximum volume, which we consider as the point in time when the transient crater is approximately reached (Elbeshausen et al., 2009; Zhu et al., 2015).

Note that the tracer method to determine the ejecta distribution does not account for structural uplift at the crater rim, which can make up to ~80% of the rim height (Sturm et al., 2016). In addition, we do not consider any ejecta sliding or late-stage modification processes. Zhu et al. (2015) have shown that the effect of sliding has little influence on the ejecta distribution. We also neglect any interaction of the ejected material with a forming vapor plume, which would accelerate especially initially ejected fast particles (Luther et al., 2019) and thus modify the deposition of very distal ejecta. Furthermore, the ejection and deposition of distal ejecta depend on the impact angle (Shuvalov, 2011). Here, we focus on distances for the ejected material where on average we do not expect significant modifications of the trajectories of the ejected material.

2.2.3. Combining Data of Melt Model and Ejecta Model

Typically, a single tracer is assigned to each cell in iSALE models. To exactly correlate the tracers in 10-CPPR ejecta models with 40-CPPR melt models, we put 16 uniformly distributed tracers in each cell of the ejecta models. Although we do not expect an increase in accuracy in the ejecta models due to a larger number of tracers, it simplifies the coupling of the shock melting models (melt models) at 40 CPPR with the crater formation and ejection models (ejecta models) at 10 CPPR. When estimating the distribution of ejected melt from ejecta models, we use the more accurate peak pressures P_{peak} from melt models for each corresponding tracer (Figure S1 in Supporting Information S1).

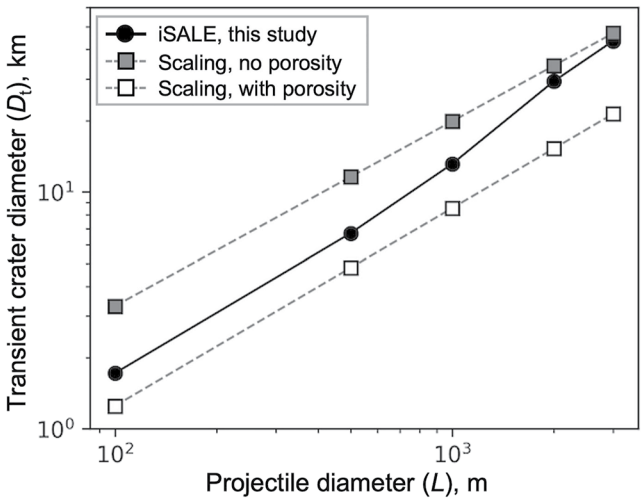

Figure 3. Determination of transient crater size. In this study, in accordance with observations (Besserer et al., 2014), we approximate the lunar stratigraphy by introducing an exponential gradient of the porosity with a porosity of ~25% at the surface and a smaller porosity at greater depths.

3. Size of Transient Crater

In our model, the transient crater size is estimated when the growing cavity reaches its maximum volume in line with previous numerical modeling (Elbeshausen et al., 2009; Zhu et al., 2015). The projectiles with a diameter of 500 m to 3 km produce craters with transient crater diameters (D_t) ranging from 1.5 to 50 km.

Using scaling laws based on impact cratering experiments (Holsapple, 1993; Schmidt & Housen, 1987) and numerical modeling (O'Keefe & Ahrens, 1993), the diameters of transient craters in nonporous targets can be calculated:

$$D_t = \frac{0.8 \cdot C_D}{1.6^{\beta}} \left(\frac{\delta}{\rho}\right)^{1/3} \frac{L^{(1-\beta)} v_i^{2\beta}}{g^{\beta}} \quad (1)$$

where g is the gravity, δ and ρ are the densities of the projectile and the target, and C_D and β are scaling parameters that depend on the target properties. For nonporous materials, C_D and β are assumed to be 1.6 and 0.22, respectively (Schmidt & Housen, 1987). We use the parameters of sand ($C_D = 1.54$ and $\beta = 0.165$, Schmidt & Housen, 1987) to calculate D_t for porous targets. As can be seen from Figure 3, our model derived D_t lies between the scaled D_t considering nonporous and porous targets. In addition, since the smaller craters formed in the shallower target with a higher porosity, their size is much closer to the scaled D_t considering porous targets.

To investigate the effects of porosity on crater sizes, Prieur et al. (2017) carried out a systematic numerical study of simple crater formation under lunar conditions in targets with varying properties. Instead of the parameter D_t, they used the dimensionless crater diameter (π_D). The parameter π_D is proportional to the ratio of the transient crater diameter and the projectile diameter. It provides insight into the efficiency to open the crater cavity while also considering the density contrast of projectile and target. Their results show that the presence of porosity causes a reduction of cratering efficiency through the compaction of pores, such that less energy is available for the crater excavation. A change in porosity from 10% to 50% causes a decrease of about ~20%–25% in π_D. Note that the calculation of D_t values of the corresponding π_D was not done because of the reduction in target density.

4. Production of Impact-Induced Melt

Scaling laws, relating impact melt volume to the initial kinetic energy of the impactor, have been developed for crystalline rocks with negligible porosity (Bjorkman & Holsapple, 1987; Pierazzo & Melosh, 2000; Pierazzo et al., 1997). They show that the volume of impact melt increases exponentially with increasing crater size in good agreement with estimated melt volumes from field observations of terrestrial craters in crystalline rocks (Grieve & Cintala, 1992). The commonly used analytical expression for melt scaling is given by a power law relationship between the volume of impact-induced melt (V_m) and D_t, is:

$$V_m = c D_t^{\,d} \quad (2)$$

where c is a material- and velocity-dependent constant, and d is a constant and is analytically defined as 3.8 (Grieve & Cintala, 1992). Wünnemann et al. (2008) investigated the effect of porosity on shock melting. They conducted a series of simulations of impacts into targets with a porosity of up to 50%. Based on the scaled D_t using Equation 1, they show D_t as a function of the volume of melt for impacts into quartzite with a porosity of 25% and into nonporous targets. Both follow a power law relationship with an exponent being identical to the analytical value (Figure 4).

According to the peak shock pressure the material has experienced, we calculate the volume of impact-induced melt. By fitting our data to Equation 2, our results (the dashed black line with black dots in Figure 4) show a gentler slope ($d = 3.09$; $c = 2.37 \times 10^{-3}$) than the analytical value. This is partially caused by the decreasing influence of the porosity gradient with increasing projectile size L. To demonstrate the significance of porosity, we conducted iSALE simulations without any target porosity (all other parameters are identical), where the critical

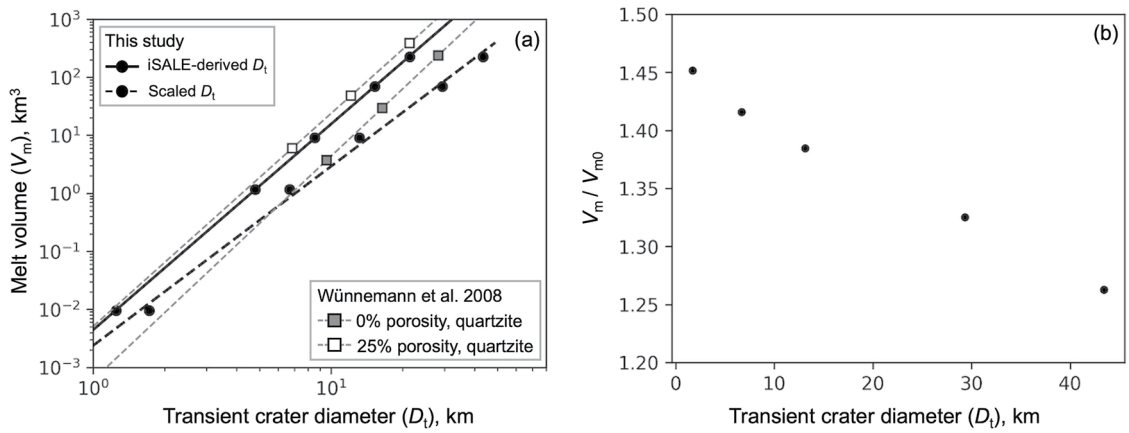

Figure 4. Melt production as a function of crater size (a) and the influence of target porosity (b). V_{m0} is the calculated volume of impact-induced melt based on simulations without any target porosity. Note that the melt volume of Wünnemann et al. (2008) was calculated based on modeling with an impact velocity of 12 km/s. For better comparison, the melt volume of Wünnemann et al. (2008) is revised by multiplying $(18\ \mathrm{km{\cdot}s^{-1}})^{1.7}/(12\ \mathrm{km{\cdot}s^{-1}})^{1.7}$ (Abramov et al., 2012).

shock pressure for melting is assumed to be 60 GPa (Hamann et al., 2016). The results (Figure 4b) show that the relative enhancement of melt abundance gradually increases with decreasing crater size, which corresponds to an increasing influence of the more porous target toward the shallowest strata (Figure 1). The smallest crater ($L = 500$ m) is formed in a depth range with the largest porosity of ~25% (Figure 1). The volume of its generated melt is ~1.45 times that produced in the target with no porosity. The largest impact ($L = 3$ km) melts the target in a depth range with the lowest porosity (Figure 1). The generated melt volume is ~1.25 times the volume that is generated in targets with no porosity.

The varying slope of the scaling lines in Figure 4 is also related to the determination of D_t. To compare with the estimates of Wünnemann et al. (2008), we replace the model-derived D_t with the scaled D_t. The results suggest an exponent $d = 3.55$ ($c = 4.41 \times 10^{-3}$) (Figure 4, the black solid line). The melt production in smaller impact events approaches the estimated values of impacts into targets of 25% porosity from Wünnemann et al. (2008), shown by the gray-dashed line with empty symbols in Figure 4. With increasing impactor size, the influence of the porosity gradient decreases and hence, the melt production approaches the estimates for a nonporous target from Wünnemann et al. (2008), shown by the gray-dashed line with filled symbols in Figure 4. The varying exponent d derived from the disparate determination of D_t highlights the importance of the determination of D_t in the scaling of melt production.

Calculated impact melt volumes generally exceed the ones measured in actual impact structures in the field (Grieve & Cintala, 1992) due to geological uncertainties (e.g., difficulties in estimating the original volume of eroded impact melts in older structures; uncertainties in estimating melt volumes in poorly exposed structures or in buried structures explored only by drilling). The modeling results are beneficial for general predictions and help to reduce such uncertainties. In addition, radar data can be useful for understanding the amount of impact-induced melt, which can be, in turn, used to better constrain the melt production. Recent Mini-RF radar data, for example, suggest that impact melt flows and ponds are more common on the Moon than was previously assumed (Carter et al., 2012).

5. Ejection of Impact-Induced Melt

5.1. Fraction of Impact-Induced Melt in Ejecta

It has long been recognized that the relative volume of impact-induced melt ejected outside the crater decreases with crater size (Cintala & Grieve, 1998; Dence, 1971). By summing up the total tracer masses of the ejected material with peak pressure P_{peak} in excess of the critical shock pressure P_c, we calculated the volume of ejected melt (V_{me}). For a given total melt production V_m, we can determine the fraction of ejected melt $f_{me} = V_{me}/V_m$. The results (Figure 5) show that relatively more melt is ejected from smaller craters than from larger ones as f_{me}

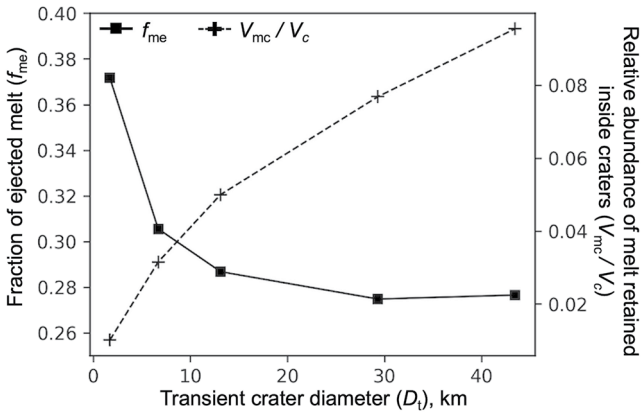

Figure 5. Distribution of impact-induced melt. The proportion of ejected melt from the total amount of melt is shown on the left *y*-axis. The fraction of melt volume retained inside the crater cavity (V_{mc}) with respect to the cavity volume (V_c) is shown on the right *y*-axis.

decreases from ~0.38 for the 1.5 km crater to ~0.28 for the 15 km crater. For the even larger craters, f_{me} decreases more slowly and levels out for craters larger than 30 km.

Cintala and Grieve (1998) used Maxwell's *Z*-model to approximate the fraction of ejected melt, where the contour of ejected material divides the melt zone into an ejected volume and a displaced volume that remains within the transient cavity (cf. Figure 2). They also show the decreasing fraction of ejected melt with crater size, but their calculated fraction, ranging from 0.6 to 0.4 for craters smaller than 50 km, is greater than our findings. The difference could be caused by the simplifications assumed by the Maxwell's *Z*-model. As Cintala and Grieve (1998) themselves state that their results from the *Z*-model are first-order estimates, simultaneous matching of depths of excavation and transient cavity radii with a single value for *z* was difficult. More importantly, their calculations do not take into account the presence of porosity, which does not only affect the total melt production, but also the displacement of shocked materials during the crater formation (cf. Figure 9 from Luther et al., 2018).

Abundant melt products, which remain inside the crater, form melt rocks. These melt products are commonly recognized as smooth melt deposits and occur as well-defined pools on the crater floor. For small craters, smaller volumes of melt are produced. Additionally, the amount of remaining melt in the crater interior is smaller. Thus, the formation of large melt pools becomes less likely because of rapid cooling. In addition, our results show the increasing abundance of melt retained inside larger craters relative to their crater volume (Figure 5), which indicate the higher probability of forming large-scale pools. Observations of lunar impact craters that display the more pervasive presence of melt pools for large craters than for smaller ones are consistent with our estimates. Using high-resolution Lunar Reconnaissance Orbiter Camera (LROC) Narrow Angle Cameras (NACs) images (0.5 m/pixel, Robinson et al., 2010), Plescia and Cintala (2012) show that a few melt deposits for small lunar craters are found to be continuous, but consist of several isolated pools. The small scale melt pools are easily obscured by regolith that has crept down the walls of the crater. Well-defined melt pools are thus only observed in fresh small craters (Plescia & Cintala, 2012).

5.2. Distribution of Ejecta Thickness

Based on scaling relationships, a theoretical expression for the thickness of the deposited ejecta (T) as a function of landing distance (r) was derived. A simple power law expression based on observations was formulated by McGetchin et al. (1973) and modified by Pike (1974):

$$T(r) = T_0(r/R_t)^{-B} \quad (3)$$

where T_0 is the thickness at the crater rim, $R_t = D_t/2$ is transient crater radius, and B is an exponent.

In Figure 6, we plot the thickness of the deposited ejecta against the radial distance normalized by the transient crater radius. To eliminate the influence of crater scale and better compare the slope, the ejecta thickness is normalized by the reference thickness T_0. The thickness of the deposited ejecta decreases with distance according to a power law with an exponent of ~−3.0, which is consistent with the laboratory experiments (Stöffler et al., 1975) and the observation of lunar ejecta blankets (McGetchin et al., 1973, $B = 3.0$). For smaller projectiles, we find that B is ~2.9. While taking into account the stronger contribution of the upper, more porous strata, it is in agreement with the results from Luther et al. (2018) for porosities of ~10%–20%. For larger projectiles, we see an increase of B, which may relate to the increasing fraction of material affected by thermal softening and melting and dimensional effects like the decreasing cratering efficiency (e.g., the distribution of relative T_0 and ejecta volume in Figures S4 and S5 in Supporting Information S1, respectively).

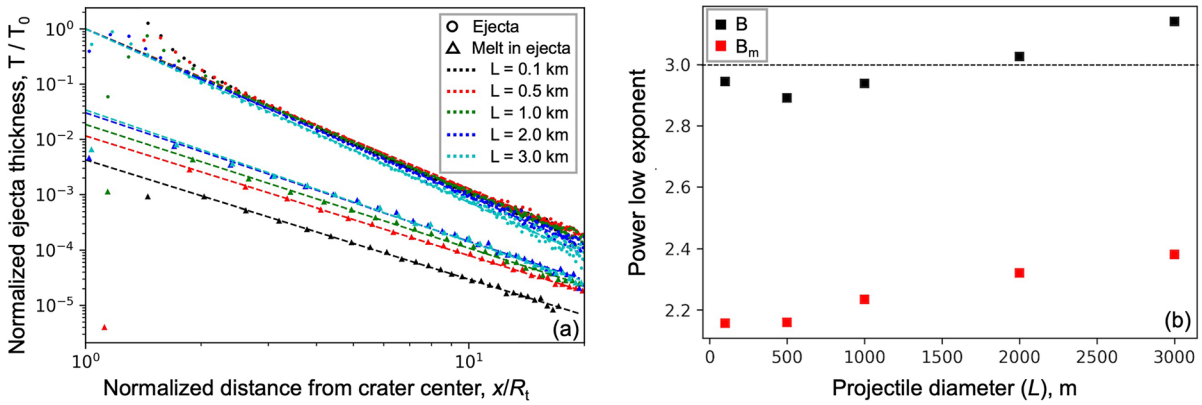

Figure 6. Ejecta thickness and melt contribution. The plot shows the distribution of ejected and molten materials (a), and the corresponding fitting results (b). In (a), both the impact-induced melt and the ejecta deposit are normalized to the same T_0 of the corresponding total blanket. In (b), the black-dashed line shows the estimate of $B = 3$ for lunar craters (McGetchin et al., 1973). The fitting parameters are also listed in Table S1 in Supporting Information S1.

5.3. Distribution of Melt Content in Ejecta

To study the melt distribution in ejected materials, we calculate the melt thickness T_m of a hypothetical "melt blanket," which only consists of impact-induced melt material. We use the same procedure as for calculating the total thickness of the ejecta blanket T, but consider only molten matter. Of course, we do not expect the molten material to compose the lower layer of the blanket, but expect that the molten material to be mixed with the total amount of ejected materials. Our simulation results (Figure 6) show that the melt thickness T_m is also a function of landing distance following a power law:

$$T_m(r) = T_{m0}(r/R_t)^{-B_m} \quad (4)$$

Similarly to the total ejecta blanket, the thickness of the melt blanket is decreasing with the distance from crater center (Figure 6). The slope of the "melt blanket" is gentler than that of the total blanket and has an exponent around −2.3. The slightly increasing value of B_m with increasing size of the projectile follows the same tendencies as the exponent of the total ejecta blanket. Using SELENE/Kaguya Terrain Camera and LROC data, Krüger et al. (2016) produced a high-resolution (10 m/pixel) map of impact melt distribution for the lunar Tycho crater. They found that the occurrence of melt ejected from Tycho crater decreases with increasing distance from the crater rim, being consistent with our estimate.

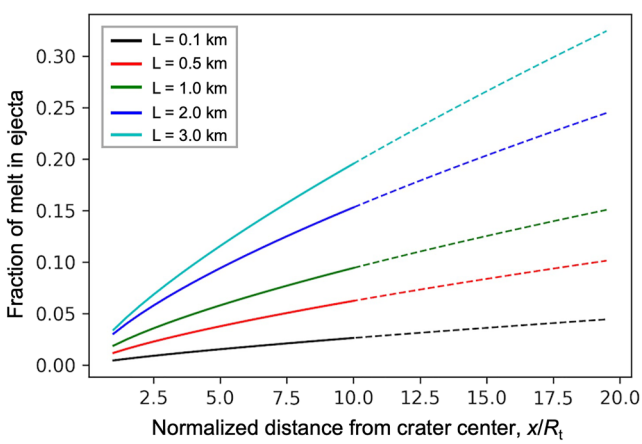

Figure 7. Concentration of melt in the ejecta blanket. Dashed lines indicate the increasing uncertainty due to the model resolution (cf. bumpy thickness in Figure 6a for x/R > 10), impact angle, and vapor plume.

Normalizing to the total thickness T_0, the results of the total ejecta blanket overlap for all projectile sizes for $x/R_t = 1$ (Figure 6). However, the ratio of T_{m0}/T_0 increases with increasing projectile size, from $\sim 3 \times 10^{-2}$ for $L = 3$ km to $\sim 4 \times 10^{-3}$ for $L = 0.1$ km (i.e., by one order of magnitude), even though cratering from the smallest projectiles results in the largest fraction of melt being ejected (Figure 5). This could result from how the ejection contour cuts through the volume of shock melt production (cf. Figure 2). Furthermore, smaller craters form in the more porous upper target lithologies, which result in the increased melt production relative to larger craters where the melting zone reaches into less porous strata. This decrease of the ratio of T_{m0}/T_0 could also be an effect of the enhanced cratering efficiency for smaller cratering events compared to larger ones (e.g., the relative ejecta volume in Figure S5 in Supporting Information S1), which causes a smaller thickness of the melt blanket relative to the total ejecta thickness for smaller projectiles.

Most of the ejected melt are distributed near the crater rim. Even though the thickness of both the ejecta and the melt blanket decreases with distance from the crater center, the decrease in total thickness is more pronounced than the melt thickness. Hence, the concentration of impact melt in the ejecta blanket increases (Figure 7). It indicates that the impact melt is highly concentrated

not only inside the crater (Figure 5) but also in the distal ejecta. These melt products have been found as millimeter-to centimeter-sized particles of pure melt that chilled rapidly to glass (e.g., Huang et al., 2018). In addition, the concentration of impact melt in the ejecta blanket increases with increasing crater size. For a 50 km crater ($L = 3$ km), the melt concentration in the blanket at 10 radii away from the crater rim is about 20%. Furthermore, we assume uniformly distributed deposits of distal ejecta, but they are usually distributed patchily and gathered in small regions, which could further enhance the concentration of melt compared to our estimates. Note that at such distances, effects from the initially fast expanding vapor plume, impact angle, or surface curvature play a role on the detailed deposition, and our results shown here have to be considered as average values.

6. Influence of Impact Angle and Velocity

Both the varying impact angle and velocity affect the production of impact melt. In this study, the distribution of melt from typical impact events with an angle of 45° at 18 km/s is considered to be representative of the majority of the intermediate-sized craters on the Moon (Shoemaker, 1962; Yue et al., 2013). The impact velocity on the Moon ranges from ∼10 km/s to >40 km/s (Yue et al., 2013). For a given size of the projectile, a higher impact velocity generates a larger amount of melt. For example, for a lunar impact with velocities from 10 km/s to 40 km/s, the volume of produced melt of a given projectile varies by several orders of magnitude (Marchi et al., 2013; Pierazzo et al., 1997). While focusing on the scaling relationship of the relative melt abundance with respect to the crater dimension, the influence of velocity on melt volume is compensated by the greater size of the crater caused by the higher impact velocity. This is consistent with analytical estimates (Abramov et al., 2012; Cintala & Grieve, 1998) that show that the melt volume can be approximated as an exponential function of merely crater size (given the density of projectile and target). In addition, using iSALE 2D hydrocodes, Luther et al. (2017) investigated the influence of impact velocity on the melt production. Their results show that, for constant kinetic energy, the melt production relative to the crater volume is generally constant for impacts with a velocity greater than ∼10 km/s. The fraction of ejected melt remains constant as well.

The impact angle also affects the melt production. In particular, very oblique impacts are thought to produce less melt. Pierazzo and Melosh (2000) found that while impacts with an angle larger than 45° generally produce comparable amounts of melt to the vertical impact case. The volume of melt for impacts at 30° drops to about 50% of the amount of melt in vertical impacts, declining to less than 10% for a 15° impact. Aside from the total melt abundance, the impact angle also influences the distribution of ejected materials, especially distal deposits (Herrick & Forsberg-Taylor, 2003; Shuvalov, 2011). Based on the observations of lunar impact craters, Herrick and Forsberg-Taylor (2003) state that while the ejecta deposits exhibit axial symmetry for impact angles >45°, the ejecta blanket of more oblique impacts becomes asymmetric. When the angle is <∼25°, a forbidden zone develops in the uprange direction of the ejecta blanket; when <∼10°, the ejecta form a "butterfly" pattern. Recently, Luo et al. (2022) used the iSALE3D hydrocodes systematically studied ejecta pattern of oblique impacts on the Moon, where the varied impact angles (10–90°), impactor diameters (1–120 km), and impact velocities (10–20 km/s) were considered. Their modeled ejecta deposits present an evolving pattern with an impact angle being consistent with the observations. In addition, they find that the impact angle under which ejecta patterns turn from symmetric to asymmetric is dependent on the impactor size.

In the distal ejecta of oblique impacts, ejecta in downrange direction should present a more pronounced melt enrichment compared with the uprange direction (Pierazzo & Melosh, 2000). The distal ejecta in downrange direction is mainly derived from high-velocity ejected particles. They are jetted from a rather shallow region of the target near the impact site that experiences the most intensive shock compression and is enriched in melt (e.g., Schultz, 1999). In addition, very oblique impacts show an enhanced amount of the heated material due to the additional shear heating of plastic work. If the shear heating is taken into account, the heated mass for an oblique impact could be comparable to a head-on impact (Manske & Wünnemann, 2022; Wakita et al., 2019). Since the shear heating mainly occurs during the late stage of crater formation, the additional heated material would mainly remain inside the crater. In addition, the influence of shear heating is significant for low-velocity impacts <10 km/s (Kurosawa & Genda, 2018; Manske et al., 2021), which is only ∼20% of the impacts on the Moon (e.g., Yue et al., 2013).

7. Implications for Interpretations of Lunar Samples

The mixing of melt products from afar is a major process that must be considered in the interpretation of sample origin. For small craters, the melt production is relatively small, but due to their great number, the contribution of melt from small craters may not be negligible. Especially in the upper shallow surface, their melt contribution could be up to 10% and the proportion of radiometrically datable melt is even higher (Liu et al., 2021). In addition, the melt concentration from small craters in distal ejecta is generally <5%. While identifying the distant-derived components in returned samples, the influence of a single small impact is not the melt of the small crater itself, but the other components in its ejecta (Korotev, 1994). Due to the heterogeneity of their occurrence regions and their high frequency, small impacts could cause a more and more complicated material composition.

For large craters, although they occur less frequently, more melt is generated and the melt concentration in distal ejecta is larger than for smaller craters: For a 50 km crater, the melt concentration in the distal ejecta ∼500 km away could be >30%. It implies that if a melt sample is supposed to be derived from a distant large crater, the location of such a crater could be extremely far away from the sampling site. In this case, we may rely on other characteristics (e.g., chemical composition) to constrain the potential origin. In addition, the proposed scaling laws to estimate melt volume and distribution as a function of impactor size are also beneficial to simulate the transport of impact melt of different ages through the cumulative impact gardening process. This study (e.g., Liu et al., 2020, 2021) provides the probability of different crater origins for a given sampling site. Being combined with chemical analysis, the modeling results can significantly narrow down the source region (Černok et al., 2021).

8. Summary

The melt distribution in ejecta of impact craters is not well quantified. To address this issue, we use iSALE 2D hydrocode to simulate the production of impact-induced melt for intermediate-sized craters. Due to the non-negligible influence of target porosity, the model includes the porosity profile of the lunar crust that was constrained by lunar gravity observations.

Following previous studies, we describe the production of impact melt in our models as a function of transient crater size according to a power law. Due to a decreasing porosity with depth in the target rocks, the melt production for small craters is more significantly enhanced compared with that for larger craters. The increasing rate of melt production with crater size is, therefore, smaller than previous estimates neglecting the effect of porosity. Care must be taken when the melt production is parameterized by a function of transient crater size D_t. Such scaling laws tend to be most sensitive to variations in D_t due to different approaches.

Some of the impact-induced melt is entrained in the ejecta flow and deposited at some distance from the crater mixed into the ejecta blanket. We investigated the dispersion of impact melt inside and outside crater structures. Our results show that with the increasing size of impact craters from 1.5 to 15 km, the ratio of ejected melt to the total melt production decreases from ∼0.4 to ∼0.3, while for even larger craters, the ratio is generally constant with a value of ∼0.28. While the thickness of both ejecta and melt blanket decreases with the distance from the crater center (following power laws), the melt concentration within the blanket is almost linearly increasing.

In the numerical models of the evolving dispersion of impact melt from large impact basins due to long-term impact gardening (Liu et al., 2020), the distribution of impact melt was an essential input. This model was developed aiming to constrain the origin of lunar samples. By using the better parameterizations of melt production from this study, the impact mixing model of Liu et al. (2020) could be enhanced.

Data Availability Statement

All data to reproduce the figures and the iSALE input files in this work can be accessed in Liu et al. (2022).

Acknowledgments
We greatly appreciate reviews from David Minton and an anonymous reviewer for insightful reviews that improved the quality of the manuscript. We acknowledge discussions about melt distribution with Natalia Artemieva. We gratefully acknowledge the developers of pySALEPlot including Tom Davison and the developers of iSALE-2D (www.isale-code.de), including Gareth Collins, Dirk Elbeshausen, Boris Ivanov, and Jay Melosh. This work was funded by the Deutsche Forschungsgemeinschaft (SFB-TRR 170/2), publication no. 167. R. L. acknowledges the funding from the European Union's Horizon 2020 research and innovation programme, NEO-MAPP, under grant agreement No. 870377. Open Access funding enabled and organized by Projekt DEAL.

References

Abramov, O., Wong, S. M., & Kring, D. A. (2012). Differential melt scaling for oblique impacts on terrestrial planets. *Icarus*, *218*(2), 906–916. https://doi.org/10.1016/j.icarus.2011.12.022

Amsden, A. A., Ruppel, H. M., & Hirt, C. W. (1980). A simplified ALE computer program for fluid flow at all speeds. LA-8095.

Artemieva, N., & Lunine, J. I. (2005). Impact cratering on Titan II. Global melt, escaping ejecta, and aqueous alteration of surface organics. *Icarus*, *175*(2), 522–533. https://doi.org/10.1016/j.icarus.2004.12.005

Barr, A. C., & Citron, R. I. (2011). Scaling of melt production in hypervelocity impacts from high-resolution numerical simulations. *Icarus*, *211*(1), 913–916. https://doi.org/10.1016/j.icarus.2010.10.022

Besserer, J., Nimmo, F., Wieczorek, M. A., Weber, R. C., Kiefer, W. S., McGovern, P. J., et al. (2014). GRAIL gravity constraints on the vertical and lateral density structure of the lunar crust. *Geophysical Research Letters*, *41*(16), 5771–5777. https://doi.org/10.1002/2014gl060240

Bjorkman, M. D., & Holsapple, K. A. (1987). Velocity scaling impact melt volume. *International Journal of Impact Engineering*, *5*(1), 155–163. https://doi.org/10.1016/0734-743X(87)90035-2

Carroll, M. M., & Holt, A. C. (1972). Static and dynamic pore-collapse relations for ductile porous materials. *Journal of Applied Physics*, *43*(4), 1626–1636. https://doi.org/10.1063/1.1661372

Carter, L. M., Neish, C. D., Bussey, D. B. J., Spudis, P. D., Patterson, G. W., Cahill, J. T., & Raney, R. K. (2012). Initial observations of lunar impact melts and ejecta flows with the Mini-RF radar. *Journal of Geophysical Research: Planets*, *117*(2), 1–13. https://doi.org/10.1029/2011JE003911

Černok, A., White, L. F., Anand, M., Tait, K. T., Darling, J. R., Whitehouse, M., et al. (2021). Lunar samples record an impact 4.2 billion years ago that may have formed the Serenitatis Basin. *Communications Earth & Environment*, *2*(1), 120. https://doi.org/10.1038/s43247-021-00181-z

Cintala, M. J., & Grieve, R. A. F. (1998). Scaling impact melting and crater dimensions: Implications for the lunar cratering record. *Meteoritics & Planetary Sciences*, *33*(4), 889–912. https://doi.org/10.1111/j.1945-5100.1998.tb01695.x

Collins, G. S., Melosh, H. J., & Ivanov, B. A. (2004). Modeling damage and deformation in impact simulations. *Meteoritics & Planetary Sciences*, *39*(2), 217–231. https://doi.org/10.1111/j.1945-5100.2004.tb00337.x

Collins, G. S., Melosh, H. J., & Wünnemann, K. (2011). Improvements to the ε-α porous compaction model for simulating impacts into high-porosity solar system objects. *International Journal of Impact Engineering*, *38*(6), 434–439. https://doi.org/10.1016/j.ijimpeng.2010.10.013

Dence, M. R. (1971). Impact melts. *Journal of Geophysical Research*, *76*(23), 5552–5565. https://doi.org/10.1029/JB076i023p05552

Elbeshausen, D., Wünnemann, K., & Collins, G. S. (2009). Scaling of oblique impacts in frictional targets: Implications for crater size and formation mechanisms. *Icarus*, *204*(2), 716–731. https://doi.org/10.1016/j.icarus.2009.07.018

Grieve, R. A. F., & Cintala, M. J. (1992). An analysis of differential impact melt-crater scaling and implications for the terrestrial impact record. *Meteoritics*, *27*(5), 526–538. https://doi.org/10.1111/j.1945-5100.1992.tb01074.x

Güldemeister, N., Wünnemann, K., Durr, N., & Hiermaier, S. (2013). Propagation of impact-induced shock waves in porous sandstone using mesoscale modeling. *Meteoritics & Planetary Sciences*, *48*(1), 115–133. https://doi.org/10.1111/j.1945-5100.2012.01430.x

Güldemeister, N., Wünnemann, K., & Poelchau, M. H. (2015). Scaling impact crater dimensions in cohesive rock by numerical modeling and laboratory experiments. *Geological Society of America Special Paper*, *518*, 17–29. https://doi.org/10.1130/2015.2518(02)

Hamann, C., Luther, R., Ebert, M., Hecht, L., Deutsch, A., Wünnemann, K., et al. (2016). Correlating laser-generated melts with impact-generated melts: An integrated thermodynamic-petrologic approach. *Geophysical Research Letters*, *43*(20), 10602–10610. https://doi.org/10.1002/2016GL071050

Herrick, R. R., & Forsberg-Taylor, N. K. (2003). The shape and appearance of craters formed by oblique impact on the Moon and Venus. *Meteoritics & Planetary Science*, *38*(11), 1551–1578. https://doi.org/10.1111/j.1945-5100.2003.tb00001.x

Holsapple, K. A. (1993). The scaling of impact processes in planetary sciences. *Annual Review of Earth and Planetary Sciences*, *21*(1), 333–373. https://doi.org/10.1146/annurev.ea.21.050193.002001

Housen, K. R., & Holsapple, K. A. (2011). Ejecta from impact craters. *Icarus*, *211*(1), 856–875. https://doi.org/10.1016/j.icarus.2010.09.017

Huang, Y.-H., Minton, D. A., Zellner, N. E. B., Hirabayashi, M., Richardson, J. E., & Fassett, C. I. (2018). No change in the recent lunar impact flux required based on modeling of impact glass spherule age distributions. *Geophysical Research Letters*, *45*(14), 6805–6813. https://doi.org/10.1029/2018GL077254

Ivanov, B. A. (2001). Mars/moon cratering rate ratio estimates. *Space Science Reviews*, *96*(1), 87–104. https://doi.org/10.1023/A:1011941121102

Ivanov, B. A., Deniem, D., & Neukum, G. (1997). Implementation of dynamic strength models into 2D hydrocodes: Applications for atmospheric breakup and impact cratering. *International Journal of Impact Engineering*, *20*(1), 411–430. https://doi.org/10.1016/S0734-743X(97)87511-2

Katz, R. F., Spiegelman, M., & Langmuir, C. H. (2003). A new parameterization of hydrous mantle melting. *Geochemistry, Geophysics, Geosystems*, *4*(9). https://doi.org/10.1029/2002GC000433

Korotev, R. L. (1994). Compositional variation in Apollo 16 impact-melt breccias and inferences for the geology and bombardment history of the Central Highlands of the Moon. *Geochimica et Cosmochimica Acta*, *58*(18), 3931–3969. https://doi.org/10.1016/0016-7037(94)90372-7

Kowitz, A., Güldemeister, N., Reimold, W. U., Schmitt, R. T., & Wünnemann, K. (2013). Diaplectic quartz glass and SiO_2 melt experimentally generated at only 5 GPa shock pressure in porous sandstone: Laboratory observations and meso-scale numerical modeling. *Earth and Planetary Science Letters*, *384*, 17–26. https://doi.org/10.1016/j.epsl.2013.09.021

Kring, D. A., & Cohen, B. A. (2002). Cataclysmic bombardment throughout the inner solar system 3.9–4.0 Ga. *Journal of Geophysical Research*, *107*(E2), 5009. https://doi.org/10.1029/2001JE001529

Krüger, T., van der Bogert, C. H., & Hiesinger, H. (2016). Geomorphologic mapping of the lunar crater Tycho and its impact melt deposits. *Icarus*, *273*, 164–181. https://doi.org/10.1016/j.icarus.2016.02.018

Kurosawa, K., & Genda, H. (2018). Effects of friction and plastic deformation in shock-comminuted damaged rocks on impact heating. *Geophysical Research Letters*, *45*(2), 620–626. https://doi.org/10.1002/2017GL076285

Liu, T., Luther, R., Manske, L., & Wünnemann, K. (2022). Melt production and ejection from lunar intermediate sized impact craters: Where is the molten material deposited? TRR170-DB. https://doi.org/10.35003/7WOWQI

Liu, T., Michael, G., Haber, T., & Wünnemann, K. (2021). formation of small craters in the lunar regolith: How do they influence the preservation of ancient melt at the surface? *Journal of Geophysical Research: Planets*, *126*(5), e2020JE006708. https://doi.org/10.1029/2020JE006708

Liu, T., Michael, G., Wünnemann, K., Becker, H., & Oberst, J. (2020). Lunar megaregolith mixing by impacts: Spatial diffusion of basin melt and its implications for sample interpretation. *Icarus*, *339*, 113609. https://doi.org/10.1016/j.icarus.2019.113609

Lompa, T., Wünnemann, K., Wahl, D., Padovan, S., & Miljković, K. (2021). Numerical investigation of lunar basin formation constrained by gravity signature. *Journal of Geophysical Research: Planets*, *126*(11), e2021JE006908. https://doi.org/10.1029/2021JE006908

Luo, X.-Z., Zhu, M.-H., & Ding, M. (2022). Ejecta pattern of oblique impacts on the Moon from numerical simulation. *LPI Contributions*, *2678*, 1133.

Luther, R., Artemieva, N., & Wünnemann, K. (2019). The effect of atmospheric interaction on impact ejecta dynamics and deposition. *Icarus*, *333*, 71–86. https://doi.org/10.1016/j.icarus.2019.05.007

Luther, R., Prieur, N. C., Wünnemann, K., & Werner, S. C. (2017). Crater formation and shock melt production for the 17th March 2013 lunar impact flash event. In *48th annual lunar and planetary science conference* (p. 3012).

Luther, R., Zhu, M. H., Collins, G., & Wünnemann, K. (2018). Effect of target properties and impact velocity on ejection dynamics and ejecta deposition. *Meteoritics and Planetary Science*, *53*(8), 1705–1732. https://doi.org/10.1111/maps.13143

Manske, L., Marchi, S., Plesa, A.-C., & Wünnemann, K. (2021). Impact melting upon basin formation on early Mars. *Icarus*, *357*, 114128. https://doi.org/10.1016/j.icarus.2020.114128

Manske, L., & Wünnemann, K. (2022). The effect of plastic work on impact-induced melting—Introducing an advanced melt quantification technique. *LPI Contributions*, *2678*, 2652.

Marchi, S., Bottke, W. F., Cohen, B. A., Wünnemann, K., Kring, D. A., McSween, H. Y., et al. (2013). High-velocity collisions from the lunar cataclysm recorded in asteroidal meteorites. *Nature Geoscience*, *6*(4), 303–307. https://doi.org/10.1038/ngeo1769

Marchi, S., Mottola, S., Cremonese, G., Massironi, M., & Martellato, E. (2009). A new chronology for the Moon and Mercury. *The Astronomical Journal*, *137*(6), 4936–4948. https://doi.org/10.1088/0004-6256/137/6/4936

McGetchin, T. R., Settle, M., & Head, J. W. (1973). Radial thickness variation in impact crater ejecta: Implications for lunar basin deposits. *Earth and Planetary Science Letters*, *20*(2), 226–236. https://doi.org/10.1016/0012-821X(73)90162-3

Melosh, H. J. (1989). *Impact cratering: A geologic process*. Oxford University.

O'Keefe, J. D., & Ahrens, T. J. (1993). Planetary cratering mechanics. *Journal of Geophysical Research*, *98*(E9), 17011–17028. https://doi.org/10.1029/93JE01330

Pierazzo, E., Artemieva, N. A., & Ivanov, B. A., (2005). Starting conditions for hydrothermal systems underneath Martian craters: Hydrocode modeling. *Large Meteorite Impacts III*, *384*, 443–457.

Pierazzo, E., & Melosh, H. J. (2000). Melt production in oblique impacts. *Icarus*, *145*(1), 252–261. https://doi.org/10.1006/icar.1999.6332

Pierazzo, E., Vickery, A. M., & Melosh, H. J. (1997). A reevaluation of impact melt production. *Icarus*, *127*(2), 408–423. https://doi.org/10.1006/icar.1997.5713

Pike, R. J. (1974). Ejecta from large craters on the Moon: Comments on the geometric model of McGetchin et al. *Earth and Planetary Science Letters*, *23*(3), 265–271. https://doi.org/10.1016/0012-821X(74)90114-9

Plescia, J. B., & Cintala, M. J. (2012). Impact melt in small lunar highland craters. *Journal of Geophysical Research: Planets*, *117*(3), 1–12. https://doi.org/10.1029/2011JE003941

Potter, R. W. K., Kring, D. A., Collins, G. S., Kiefer, W. S., & McGovern, P. J. (2013). Numerical modeling of the formation and structure of the Orientale impact basin. *Journal of Geophysical Research: Planets*, *118*(5), 963–979. https://doi.org/10.1002/jgre.20080

Prieur, N. C., Rolf, T., Luther, R., Wünnemann, K., Xiao, Z., & Werner, S. C. (2017). The effect of target properties on transient crater scaling for simple craters. *Journal of Geophysical Research: Planets*, *122*(8), 1704–1726. https://doi.org/10.1002/2017JE005283

Quintana, S. N., Crawford, D. A., & Schultz, P. H. (2015). Analysis of impact melt and vapor production in CTH for planetary applications. *Procedia Engineering*, *103*, 499–506. https://doi.org/10.1016/j.proeng.2015.04.065

Raducan, S. D., Davison, T. M., Luther, R., & Collins, G. S. (2019). The role of asteroid strength, porosity and internal friction in impact momentum transfer. *Icarus*, *329*, 282–295. https://doi.org/10.1016/j.icarus.2019.03.040

Robinson, M. S., Brylow, S. M., Tschimmel, M., Humm, D., Lawrence, S. J., Thomas, P. C., et al. (2010). Lunar reconnaissance orbiter camera (LROC) instrument overview. *Space Science Reviews*, *150*(1–4), 81–124. https://doi.org/10.1007/s11214-010-9634-2

Schmidt, R. M., & Housen, K. R. (1987). Some recent advances in the scaling of impact and explosion cratering. *International Journal of Impact Engineering*, *5*(1), 543–560. https://doi.org/10.1016/0734-743X(87)90069-8

Schultz, P. H. (1999). Ejecta distribution from oblique impacts into particulate targets. In *Lunar and planetary science conference* (p. 1919).

Shoemaker, E. M. (1962). Interpretation of lunar craters. In *Physics and astronomy of the Moon* (pp. 283–359). Elsevier. https://doi.org/10.1016/B978-1-4832-3240-9.50012-2

Shuvalov, V. (2011). Ejecta deposition after oblique impacts: An influence of impact scale. *Meteoritics & Planetary Science*, *1718*(11), 1713–1718. https://doi.org/10.1111/j.1945-5100.2011.01259.x

Stöffler, D. (2006). Cratering history and lunar chronology. *Reviews in Mineralogy and Geochemistry*, *60*(1), 519–596. https://doi.org/10.2138/rmg.2006.60.05

Stöffler, D., Gault, D. E., Wedekind, J., & Polkowski, G. (1975). Experimental hypervelocity impact into quartz sand: Distribution and shock metamorphism of ejecta. *Journal of Geophysical Research*, *80*(29), 4062–4077. https://doi.org/10.1029/JB080i029p04062

Sturm, S., Kenkmann, T., & Hergarten, S. (2016). Ejecta thickness and structural rim uplift measurements of Martian impact craters: Implications for the rim formation of complex impact craters. *Journal of Geophysical Research: Planets*, *121*(6), 1026–1053. https://doi.org/10.1002/2015JE004959

Vaniman, D., Dietrich, J., Taylor, G. J., & Heiken, G. (1991). Exploration, samples, and recent concepts of the Moon. In G. H. Heiken, D. T. Vaniman, & B. M. French (Eds.), *Lunar source-book: A user's guide to the Moon* (pp. 5–26). Cambridge University Press.

Wakita, S., Genda, H., Kurosawa, K., & Davison, T. M. (2019). Enhancement of impact heating in pressure-strengthened rocks in oblique impacts. *Geophysical Research Letters*, *46*(23), 13678–13686. https://doi.org/10.1029/2019GL085174

Wünnemann, K., Collins, G. S., & Melosh, H. J. (2006). A strain-based porosity model for use in hydrocode simulations of impacts and implications for transient crater growth in porous targets. *Icarus*, *180*(2), 514–527. https://doi.org/10.1016/j.icarus.2005.10.013

Wünnemann, K., Collins, G. S., & Osinski, G. R. (2008). Numerical modelling of impact melt production in porous rocks. *Earth and Planetary Science Letters*, *269*(3), 530–539. https://doi.org/10.1016/j.epsl.2008.03.007

Wünnemann, K., Zhu, M.-H., & Stöffler, D. (2016). Impacts into quartz sand: Crater formation, shock metamorphism, and ejecta distribution in laboratory experiments and numerical models. *Meteoritics and Planetary Science*, *51*(10), 1762–1794. https://doi.org/10.1111/maps.12710

Yue, Z., Johnson, B. C., Minton, D. A., Melosh, H. J., Di, K., Hu, W., & Liu, Y. (2013). Projectile remnants in central peaks of lunar impact craters. *Nature Geoscience*, *6*(6), 435–437. https://doi.org/10.1038/ngeo1828

Zhu, M.-H., Wünnemann, K., & Artemieva, N. (2017). Effects of Moon's thermal state on the impact basin ejecta distribution. *Geophysical Research Letters*, *44*(22), 11292–11300. https://doi.org/10.1002/2017GL075405

Zhu, M.-H., Wünnemann, K., & Potter, R. W. K. (2015). Numerical modeling of the ejecta distribution and formation of the Orientale basin on the Moon. *Journal of Geophysical Research: Planets*, *120*(12), 2118–2134. https://doi.org/10.1002/2015JE004827